HHS Public Access

Author manuscript

Dev Cell. Author manuscript; available in PMC 2024 March 13.

Published in final edited form as:

Dev Cell. 2023 March 13; 58(5): 338–347.e4. doi:10.1016/j.devcel.2023.02.002.

Plasticity in airway smooth muscle differentiation during mouse lung development

Katharine Goodwin[1], **Bezia Lemma**[2], **Pengfei Zhang**[2,3], **Adam Boukind**[3], **Celeste M. Nelson**[2,3,*]

[1]Lewis-Sigler Institute for Integrative Genomics, Princeton University, Princeton, NJ 08544, USA

[2]Department of Chemical and Biological Engineering, Princeton University, Princeton, NJ 08544, USA

[3]Department of Molecular Biology, Princeton University, Princeton, NJ 08544, USA

Summary

Smooth muscle differentiation has been proposed to sculpt airway epithelial branches in mammalian lungs. Serum response factor (SRF) acts with its cofactor myocardin to activate expression of contractile smooth muscle markers. In the adult, however, smooth muscle exhibits a variety of phenotypes beyond contractile that are independent of SRF/myocardin-induced transcription. To determine whether a similar phenotypic plasticity is exhibited during development, we deleted *Srf* from the mouse embryonic pulmonary mesenchyme. *Srf*-mutant lungs branch normally and the mesenchyme displays mechanical properties indistinguishable from controls. scRNA-seq identified an *Srf*-null smooth muscle cluster wrapping the airways of mutant lungs that lacks contractile smooth muscle markers but retains many features of control smooth muscle. *Srf*-null embryonic airway smooth muscle exhibits a synthetic phenotype, compared to the contractile phenotype of mature wildtype airway smooth muscle. Our findings identify plasticity in embryonic airway smooth muscle, and demonstrate that a synthetic smooth muscle layer promotes airway branching morphogenesis.

Graphical Abstract

*Lead contact: celesten@princeton.edu.

Author contributions: K.G. and C.M.N. conceptualized the study, designed the experiments, interpreted the data, and wrote the manuscript. K.G., B.L., A.B., and P.Z. performed the experiments and collected the data. All authors provided input on the final manuscript.

Declaration of interests: The authors declare no competing interests.

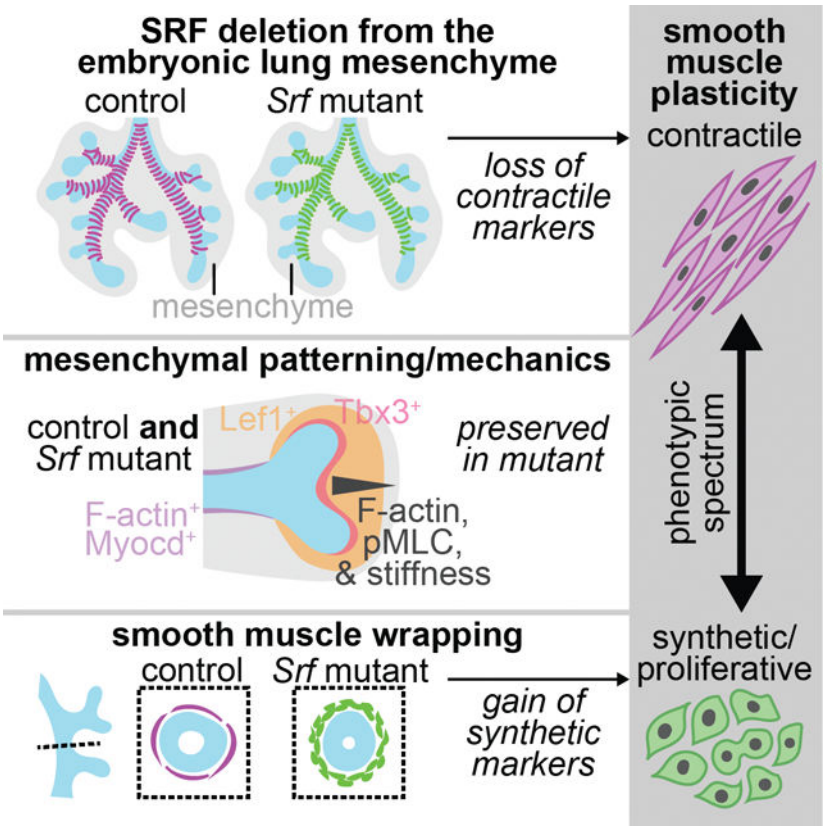

eTOC blurb

Deletion of myogenic transcription factors leads to loss of contractile smooth muscle markers without affecting branching of the embryonic mouse lung. Goodwin et al. show that these mutant lungs contain a smooth muscle population that expresses synthetic smooth muscle markers, wraps the airways, and is sufficient to support branching morphogenesis.

Keywords

morphodynamics; mechanobiology; stiffness

Introduction

Vascular and visceral smooth muscle cells are present throughout the body and their differentiation is key for development and homeostasis[1,2]. In the adult, smooth muscle takes on contractile or synthetic/proliferative phenotypes in response to local signals[3–5]. For vascular smooth muscle, scRNA-seq analysis has identified at least six phenotypes[6]. Studies using cultured cells have implicated myocardin, acting with its required co-factor, serum response factor (SRF), as a key transcriptional activator of contractile smooth muscle markers[7–9], including *Acta2* (α-smooth muscle actin; αSMA), *Tagln* (transgelin, SM22α), and *Cnn1* (calponin-1). Changes in *Myocd* expression are associated with cardiovascular

disease, and downregulation of *Myocd* can cause an osteogenic phenotype in vascular smooth muscle and subsequent arterial calcification in patients with type 2 diabetes[10].

SRF-deficient embryos die at embryonic day 6.5 (*E*6.5) from a defect in gastrulation due to a complete loss of mesenchymal cells[11]. Myocardin (*Myocd*)−/− animals die at *E*10.5 because of vascular abnormalities[12]. Injecting *Myocd*−/− embryonic stem cells into wildtype blastocysts showed that wildtype cells can outcompete myocardin-null cells in visceral smooth muscle, but less so in vascular smooth muscle[13]. SRF/myocardin signaling was therefore concluded to be essential for visceral smooth muscle differentiation. Nonetheless, mice deficient in *Acta2*, *Tagln*, or *Cnn1* are all viable[14–16], suggesting that these SRF/myocardin targets are dispensable for smooth muscle differentiation.

The airway smooth muscle differentiation program is just beginning to be defined. Multiple signaling pathways affect each step of the process, from regulating the pool of smooth muscle progenitors, to specifying nascent smooth muscle cells, to inducing their differentiation and maturation[17]. Importantly, cytoskeletal and adhesion genes are expressed before contractile smooth muscle markers, suggesting early changes to the mechanical properties of the mesenchyme as it begins to differentiate into smooth muscle. Disrupting the smooth muscle differentiation program leads to defective branching morphogenesis of the epithelium, with a loss of smooth muscle differentiation associated with cystic branches and a gain associated with stunted branches[17–23]. These observations have led to a conceptual model wherein the pulmonary mesenchyme sculpts the morphology and positions of branches that form in the growing airway epithelium[1].

However, recent work in which *Myocd* was deleted from the embryonic pulmonary mesenchyme appears to cast doubt on this model. *Myocd*-mutant lungs fail to express markers of contractile smooth muscle but branch normally[24]. That study did not determine whether loss of Myocd affects the entire smooth muscle differentiation program, raising the possibility that early stages of smooth muscle differentiation (which sculpt new epithelial branches and occur prior to robust *Myocd* expression) are unaffected by loss of *Myocd*, and/or that *Myocd*-independent aspects of the smooth muscle transcriptome are sufficient to support epithelial morphogenesis. Here, we sought to resolve these seemingly contradictory observations and define precisely the role of SRF/myocardin-induced transcription in the embryonic pulmonary mesenchyme.

Results

Deleting Srf from the embryonic pulmonary mesenchyme permits airway branching

To understand the role of SRF/myocardin-induced transcription in airway smooth muscle differentiation and morphogenesis in the embryonic mouse lung, we deleted *Srf* from the pulmonary mesenchyme using *Tbx4-rtTA;tet-O-Cre*[25]. This strategy allows for doxycycline-induced activation of Cre recombinase exclusively in the pulmonary mesenchyme by using a tissue-specific enhancer of *Tbx4*. Immunofluorescence analysis for E-cadherin (Ecad) and αSMA showed that deleting *Srf* from the pulmonary mesenchyme results in a normally branched airway epithelial tree devoid of αSMA^+ cells at *E*12.5 (Fig. 1A–B). The number of terminal branches is similar in *Srf*-mutant and littermate control lungs (Fig. 1C), as is the

size of the lungs (Fig. S1A–D). However, *Srf*-mutant lungs have significantly smaller caliber airways than controls (Fig. 1D).

We used timelapse imaging of lungs cultured *ex vivo* to visualize the dynamics of branching morphogenesis and airway smooth muscle contractions (Fig. 1E). Bifurcation of the airway epithelium proceeds at the same rate in *Srf* mutants as in controls (Fig. 1F), consistent with their ability to form a normal number of branches. However, *Srf*-mutant airways lack spontaneous contractile behaviors (Fig. 1G; Movie S1). These observations are similar to previous descriptions of lungs from mice in which the SRF cofactor *Myocd* had been deleted from the embryonic pulmonary mesenchyme[24]. Combined with that work, our data suggest that SRF/myocardin-dependent genes are not required in the pulmonary mesenchyme for airway epithelial branching.

Srf-mutant lungs have normal mesenchymal patterning and mechanical properties

Given that deleting *Srf* from the mesenchyme has no effect on epithelial morphogenesis, we next focused our attention on the mesenchyme itself to characterize the phenotype of this mutant. Specifically, we evaluated the patterning and mechanical properties of the mesenchyme in *E*12.5 *Srf*-mutant lungs. In wildtype lungs, the branching epithelium is surrounded by sub-epithelial mesenchymal cells that express lymphoid enhancer binding factor 1 (Lef1) and bone morphogenetic protein 4 (Bmp4) (Fig. 2A)[17]. Immunofluorescence and RNAscope analysis showed that Lef1 and Bmp4 are expressed in similar patterns in *Srf*-mutant lungs and controls (Fig. 2B–D), indicating that *Srf* is dispensable for patterning the sub-epithelial mesenchyme. In wildtype lungs, nascent smooth muscle cells immediately adjacent to the epithelium express T-box transcription factor 3 (Tbx3)[17]. Immunofluorescence analysis showed that Tbx3 is also expressed in the mesenchyme adjacent to the epithelium in *Srf* mutants (Fig. 2E–F), suggesting that SRF is similarly dispensable for specifying the earliest stages of airway smooth muscle differentiation.

Deposition of the extracellular matrix protein fibronectin has been proposed to play a role in cleft formation during bifurcation of the airway epithelium[26,27]. We examined the distribution of fibronectin in *Srf* mutants and controls at *E*12.5 and found no differences at epithelial bifurcation points (Fig. S1E–F), showing that loss of *Srf* has no effect on fibronectin deposition in the mouse lung. These data suggest that alterations in fibronectin do not provide a compensatory mechanism to drive branching in the absence of contractile smooth muscle proteins.

Filamentous actin (F-actin) and phosphorylated myosin light chain (pMLC) are molecular markers associated with the mechanical properties of airway smooth muscle – specifically, enhanced stiffness and mechanical tone[28–30]. Consistently, the levels of F-actin and pMLC are enriched in the mesenchyme immediately adjacent to epithelial tips, sites of active branching morphogenesis, and decrease farther from the epithelium (Fig. 2G–J). We observed similar patterns of F-actin and pMLC in *Srf* mutants (Fig. 2G–J). The highest levels of F-actin are concentrated in the mesenchyme wrapping around epithelial branches in both controls and mutants (Fig. 2K–L), despite loss of αSMA in the latter (Fig. 2M). These patterns of F-actin and pMLC correlate with levels of cortical tension in the embryonic pulmonary mesenchyme previously inferred using a FRET-based tension

sensor[17]. Therefore, loss of SRF does not reduce the stiffness or mechanical tone of the pulmonary mesenchyme.

Based on the normal patterning of these molecular markers of mechanical stiffness and tone, we hypothesized that the *Srf*-null mesenchyme remains capable of mechanically sculpting the airway epithelium. To test this hypothesis, we compared the morphology of epithelial bifurcations before and after surgically removing the surrounding mesenchyme. In both mutants and controls, the depth of the cleft at bifurcations significantly decreases following removal of the mesenchyme (Fig. S1G–H). Importantly, cleft depths in *Srf* mutants are initially indistinguishable from those in controls, and they decrease to identical levels after removing the mesenchyme. We also carried out atomic force microscopy (AFM) measurements and found similar patterns of elastic moduli in the mesenchyme of *Srf*-mutant and control lungs (Fig. 2N, Fig. S1I–K). Based on these data, we conclude that *Srf* is not required for patterning the molecular or passive mechanical features of the embryonic pulmonary mesenchyme. Consequently, mesenchymal sculpting of the epithelium is independent of *Srf*-induced transcription.

scRNA-seq of Srf-mutant lungs identifies a “smooth muscle-like” population of cells

Given that deleting *Srf* does not affect mesenchymal patterning around the airway epithelium, we used single-cell transcriptomics to broadly characterize the changes induced by loss of *Srf*. We generated scRNA-seq datasets from whole *Tbx4-rtTA;tet-O-Cre;Srf*$^{fl/fl}$ lungs and *Srf*$^{fl/fl}$ controls isolated at *E*12.5 (Fig. 3A). Both datasets contained the expected populations of cells, including mesenchyme, epithelium, vascular endothelium, mesothelium, neurons, and immune cells (Fig. 3A, Fig. S2A). Consistent with our immunofluorescence analysis, the SRF-induced contractile smooth muscle markers *Acta2* and *Tagln* were detected in the smooth muscle cluster of the control dataset (cluster 7) and were absent from the mutant dataset (Fig. 3B). *Srf* was detected throughout the control mesenchyme and absent from the mutant mesenchyme, confirming that mesenchymal expression of Cre resulted in the expected knockout (Fig. 3C). *Myocd* was present in the smooth muscle cluster in the control dataset, as expected, but was also expressed at high levels in cluster 9 of the mutant dataset (Fig. 3C). As compared to the smooth muscle cluster in the control, cells in mutant cluster 9 expressed significantly lower levels of canonical markers of contractile smooth muscle, including *Acta2*, *Tagln*, *Cnn1*, *Myl9*, and *Myh11* (Fig. S2B–F). This *Myocd*$^{+}$ cluster also did not contain *Srf*-expressing cells (Fig. 3C, Fig. S2G), ruling out the possibility of a failure in Cre-mediated recombination. As an alternate approach, we integrated the control and *Srf*-mutant datasets and visualized the resultant clusters (Fig. S2H). Both control and *Srf*-mutant cells were present in all clusters (Fig. S2I), including a *Myocd*-enriched cluster that also contained *Acta2*$^{+}$ and *Tagln*$^{+}$ cells (Fig. S2J–L). This analysis suggests that *Srf*-mutant lungs contain cells that are transcriptionally similar to wildtype smooth muscle, albeit lacking the expression of contractile markers.

To map the locations of the *Myocd*$^{+}$ clusters, we carried out RNAscope analysis of *Acta2* and *Myocd*. In control lungs, *Acta2* and *Myocd* expression showed close spatial overlap in cells adjacent to the epithelium, as expected for markers of airway smooth muscle (Fig. 3D). In contrast, *Srf*-mutant lungs lacked *Acta2* expression, in agreement with our

immunofluorescence and scRNA-seq analyses. Nonetheless, the mutants exhibited clear *Myocd* expression in the same pattern as controls. *Srf*-mutant lungs thus contain *Myocd*$^{+}$ cells that wrap the airways in a pattern indistinguishable from that of airway smooth muscle. Therefore, a "smooth muscle" cluster persists in lungs lacking mesenchymal *Srf*. Consistent with this conclusion, our scRNA-seq data showed that many *Srf*-independent smooth muscle markers are expressed in the smooth muscle clusters of both control and *Srf*-mutant lungs (Fig. 3E).

To define the extent to which *Srf*-null smooth muscle is functionally similar to control smooth muscle, we carried out KEGG pathway enrichment analysis on marker genes for each smooth muscle cluster. Signaling pathways related to cell mechanical properties and cell signaling were similarly enriched in both control and *Srf*-null smooth muscle (Fig. 3F, Fig. S3). Among the pathways unique to control smooth muscle were "vascular smooth muscle contraction" and "gap junctions", suggesting that smooth muscle maturation may be impaired in *Srf* mutants (Fig. 3F, Fig. S3), in agreement with the loss of spontaneous contractions (Fig. 1G). Consistently, we found that genes under the KEGG term "signaling pathways regulating the pluripotency of stem cells" were enriched in only the mutant smooth muscle cluster (Fig. 3F, Fig. S3). These data show that deleting *Srf* from the embryonic pulmonary mesenchyme is not sufficient to eliminate airway smooth muscle per se. Instead, SRF-induced signaling appears to affect a minor subset of genes, including contractile smooth muscle markers.

Srf-null embryonic airway smooth muscle cells are phenotypically similar to adult synthetic smooth muscle

Pearson correlation analysis of each pair of clusters shows a high degree of similarity between the mesenchyme of control and *Srf*-mutant lungs, with strong correlations observed between undifferentiated mesenchymal cells, smooth muscle cells, and cartilage precursors of both genotypes (Fig. S4A). This analysis also identified similarities between mutant smooth muscle and control cartilage precursors (asterisks in Fig. S4A). Alcian blue staining showed no ectopic cartilage around the airways of *Srf*-mutant lungs at *E*18.5 (Fig. S4B–C), demonstrating that *Srf*-null smooth muscle does not differentiate into cartilage. This analysis also identified stronger correlations between undifferentiated mesenchyme and mutant smooth muscle compared to control smooth muscle (dashed boxes in Fig. S4A). We therefore asked whether *Srf*-null smooth muscle cells resemble nascent (immature) control smooth muscle, or whether they differentiate down a different trajectory. We carried out diffusion analysis[31] of control mesenchymal cells, which showed that the trajectory of undifferentiated mesenchyme bifurcates into either smooth muscle or cartilage precursors (Fig. 4A, left). Diffusion analysis of mutant cells showed separation of the smooth muscle cluster from the rest of the mesenchyme (Fig. S4C), but the separation was less pronounced than that observed in the control dataset, consistent with our hypothesis that *Srf*-null smooth muscle remains immature. We then projected the *Srf*-null smooth muscle cells onto the control diffusion map (Fig. 4A, right). Mutant smooth muscle cells clustered among the undifferentiated mesenchymal cells near the bifurcation point between the smooth muscle and cartilage precursor branches. These results suggest that *Srf*-null smooth muscle may be

trapped in the earliest stages of smooth muscle differentiation and prevented from maturing into a contractile phenotype.

To test the plausibility of this hypothesis, we compiled a list of genes that serve as markers for contractile and synthetic adult smooth muscle[1,3,6,32–34] and clustered *Srf*-mutant and control embryonic airway smooth muscle cells based on their expression of these genes (Fig. 4B, Fig. S4E, Table S1). Contractile and synthetic markers tend to cluster together, as do mutant and control smooth muscle. Consistent with our hypothesis, contractile markers are strongly enriched in control smooth muscle (Fig. 4B, Fig. S4E). In contrast, some synthetic markers are strongly enriched in *Srf*-null smooth muscle (*Col2a1*, *Sox9*, and *Vcan*), whereas others show a more modest enrichment (*Bgn*, *Fn1*, *Sox5*, *Sox6*, *Tgfb3*, *Dcn*, *Runx2*, and *Sorbs3*). These data suggest that wildtype (mature) embryonic airway smooth muscle exhibits a classical contractile phenotype. In contrast, the gene-expression program of *Srf*-null (immature) embryonic airway smooth muscle is more consistent with a classical synthetic phenotype.

We confirmed these observations using immunofluorescence and RNAscope analysis for markers of synthetic smooth muscle (Sox9 and Col21a1) and cell proliferation (Ki67 and EdU incorporation). We observed dense accumulation of $Sox9^+$ cells in the mesenchyme around the epithelium of *Srf*-mutant lungs, but not controls (Fig. 4C–D). Additionally, the $Sox9^+$ cell layer in mutants is significantly thicker than the αSMA^+ cell layer in controls (Fig. 4E). *Col2a1* is present in the epithelium and in cartilage precursors lining the lateral side of the upper primary bronchi in both controls and mutants (Fig. 4F), as expected given its known gene-expression patterns[35,36]. Additionally, we found that *Col2a1* is expressed in $Acta2^{-}Myocd^{+}$ mutant smooth muscle cells but not $Acta2^{+}Myocd^{+}$ controls (Fig. 4F). Ki67 expression and EdU incorporation are higher in the smooth muscle cells of the mutant compared to the control, suggesting that more *Srf*-null smooth muscle cells are actively proliferating (Fig. 4G–J). Consistently, cell-cycle scoring of our scRNA-seq data showed that more cells of the control are in G1 phase whereas more cells of the mutant are in S phase (Fig. 4K). Given that *Srf*-null smooth muscle expresses Sox9 and Col2a1 and is highly proliferative, we conclude that the loss of SRF arrests this population in a synthetic smooth muscle state. Therefore, we conclude that *Srf* promotes the contractile phenotype in embryonic airway smooth muscle.

Discussion

The airway epithelium branches normally in embryos lacking *Srf* in the pulmonary mesenchyme. Consistently, *Srf*-null mesenchyme displays normal patterning and passive mechanical properties during the early stages of lung development. Close inspection uncovered that *Srf*-mutant lungs contain a population of smooth muscle cells that lacks classical markers of contractile smooth muscle but that is otherwise transcriptionally and functionally similar to control smooth muscle. This *Srf*-null population resembles immature smooth muscle and displays markers of the classical synthetic/proliferative smooth muscle phenotype described in adult tissues, suggesting that embryonic airway smooth muscle matures along a continuum from synthetic to contractile states. Phenotyping switching

of smooth muscle in the adult might therefore represent a reactivation/reversal of normal embryonic programming.

Our findings demonstrate that SRF-independent aspects of airway smooth muscle differentiation are sufficient to support epithelial branching. Since these early stages are the important sculptors of the airway epithelium (and not the later stages of smooth muscle maturation)[21,23], it is unsurprising that SRF/myocardin-induced transcription is dispensable for branching morphogenesis in the lung. *Srf* (or *Myocd*) deletion leads to only a subtle change in epithelial morphology: a narrowing of branch stalks, despite loss of the contractile smooth muscle phenotype (Fig. 1D)[24]. Our results provide an explanation for this seemingly contradictory observation. Accumulation of proliferative synthetic smooth muscle may constrain the airways simply by wrapping the epithelium with a larger number of cells with elevated stiffness and mechanical tone, without the need for contractile smooth muscle machinery. This concept is illustrated by reconstructed cross-sections through the airways, which show that a dense layer of $Sox9^+$ cells encircles the epithelium in the mutant, twice as thick as the layer of αSMA^+ cells in the control (Fig. 4C, E).

The physical mechanisms of branching of the mammalian lung and, in particular, the role of mechanical forces from smooth muscle, have been debated due to seemingly contradictory findings[21,23,24]. Our results suggest that synthetic smooth muscle provides its adjacent epithelium with a similar mechanical constraint as contractile smooth muscle. As a result, this phenotypic switch in smooth muscle has no consequence for branching morphogenesis in the embryonic mouse lung. The conceptual model wherein localized smooth muscle differentiation from the embryonic pulmonary mesenchyme sculpts epithelial branches therefore holds. Future studies are needed to determine whether a synthetic smooth muscle phenotype is conserved during the development of other embryonic organs.

Limitations of the study

Our analysis was based on the expression of marker genes compiled from datasets of adult smooth muscle. The nature of embryonic smooth muscle and whether it exhibits contractile and synthetic phenotypes in other contexts warrants further investigation.

STAR Methods

RESOURCE AVAILABILITY

Lead Contact

- Further information and requests for resources and reagents should be directed to and will be fulfilled by the lead contact, Celeste M. Nelson (celesten@princeton.edu).

Materials availability

- This study did not generate new unique reagents.

Data and code availability

- Single-cell RNA-seq data have been deposited at GEO. Accession numbers are listed in the key resources table.
- This paper does not report original code.
- Any additional information required to reanalyze the data reported in this paper is available from the lead contact upon request.

EXPERIMENTAL MODEL AND SUBJECT DETAILS

Mice—All procedures involving animals were approved by Princeton University's Institutional Animal Care and Use Committee. Mice were housed in an AAALAC-accredited facility in accordance with the NIH Guide for the Care and Use of Laboratory Animals. This study was compliant with all relevant ethical regulations regarding animal research. Srf-flox (Jackson Laboratory Stock 006658), Rosa26-mTmG (Jackson Laboratory Stock 007676), and Tbx4-rtTA;tet-O-Cre[25] (gift of Dr. Wei Shi) mice were used to generate *Srf-flox; mTmG* embryos and to delete *Srf* from the embryonic pulmonary mesenchyme. Doxycycline was administered in drinking water at 0.5 mg/ml starting at *E*5.5 or *E*6.5. Genotyping was carried out by isolating DNA from ear punches of pups or from the head of each embryo, followed by PCR and gel electrophoresis. In experiments using *Srf-flox;mTmG* mice, Cre and Tbx4 genotype was determined by the presence of GFP. The primer sequences for Cre were GCATTACCGGTCGATGCAACGAGTGATGAG and GAGTGAACGAACCTGGTCGAAATCAGTGCG, and the primer sequences for Tbx4-rtTA were GGAAGGCGAGTCATGGCAAGA and AGGTCAAAGTCGTCAAGGGCA. The primer sequences for Srf-flox and mTmG are all provided on the Jackson Laboratory website.

METHOD DETAILS

Wholemount immunofluorescence staining and imaging—Isolated lungs were fixed in 4% paraformaldehyde in PBS for 30 minutes at 4°C. Lungs were washed four times for 15 minutes with PBST (0.1% Triton X-100 in PBS) and then blocked with 5% goat serum and 0.1% BSA for one hour. Samples were then incubated with primary antibodies against αSMA (Sigma a5228, 1:400 or Abcam ab5694, 1:200), E-cadherin (Cell Signaling 3195, 1:200 or Invitrogen 13–1900, 1:200), fibronectin (Invitrogen PA5-29578, 1:200), Lef1 (Cell Signaling 2230, 1:200), Ki67 (Abcam a15580, 1:200), pMLC2 (Cell Signaling 3671, 1:200), RFP (Abcam ab62341, 1:400), Sox9 (Sigma AB5535, 1:1000), or Tbx3 (Invitrogen 42–4800, 1:200), followed by incubation with Alexa Fluor-conjugated secondary antibodies (1:400; Thermo Fisher Scientific A11007, A21244, A11012, A21240 and A11006) or Alexa Fluor-conjugated phalloidin (1:400, Thermo Fisher Scientific A12380 or A12379) and then counterstained with Hoechst (1:1000). Lungs were dehydrated in a methanol or isopropanol (for phalloidin-stained samples) series and cleared with Murray's clear (1:2 ratio of benzyl alcohol to benzyl benzoate). Samples were imaged using a spinning disk confocal (BioVision X-Light V2) fitted to an inverted microscope.

Fluorescence in situ hybridization—Isolated lungs were immediately placed in freshly prepared 4% paraformaldehyde in PBS for 24 hours at 4°C. Lungs were then washed

in PBS, followed by 20% sucrose and then 30% sucrose in PBS at 4°C until they sank (less than 24 hours). All reagents were prepared using autoclaved and RNaseZAP-treated (Sigma R2020) water. Lungs were then embedded in OCT (Tissue Tek), frozen on dry ice, and stored at −80°C. Sectioning was performed on a Leica CM3050S cryostat. Sample blocks were equilibrated at −20°C in the cryostat for 1 hour and then sliced into 10-μm-thick sections onto Superfrost Plus slides (Fisherbrand). Fluorescence in situ hybridization was performed using the standard RNAScope Multiplex Fluorescent V2 Assay (ACD) protocol for fixed-frozen samples. Probes used were for *Mus musculus Myocd* (channel 1, 581051), *Col2a1* (channel 2, 407221), *Bmp4* (channel 2, 401301), and *Acta2* (channel 3, 319531). Fluorophores were Opal 520 and Opal 620 (Akoya Biosciences FP1487001KT and FP1495001KT). Sections were imaged on a Nikon A1RSi confocal microscope with a 20× objective.

Organ culture and live imaging of contractions—Lung explants were cultured *ex vivo* following established protocols[37]. Lungs were dissected in cold PBS supplemented with antibiotics (50 units/ml of penicillin and streptomycin) and cultured on porous membranes (nucleopore polycarbonate track-etch membrane, 8 μm pore size, 25 mm diameter; Whatman) floating on DMEM/F12 medium (without HEPES) supplemented with 5% fetal bovine serum (FBS, heat inactivated; Atlanta Biologicals) and antibiotics (50 units/ml of penicillin and streptomycin) within a glass-bottom dish. Lungs were cultured within a stage-top incubator (Pathology Devices) on an inverted microscope (Nikon Ti) and imaged under brightfield (1–2 ms exposure). Every hour for 12 hours, a five-minute timelapse was taken with frames acquired every three seconds. Timelapses from hours 6 to 12 were analyzed for the presence of spontaneous smooth muscle contractions, visible by deformations of the epithelium, and compared using a two-sided t-test in GraphPad Prism. For EdU incorporation experiments, we first cultured *E*12.5 lungs on porous membranes for 1 hour and then added EdU to the culture medium for 15 minutes prior to fixation and subsequent reactions using the Click-iT EdU Alexa Fluor 488 Kit (Thermo Fisher Scientific).

scRNA-seq experiments—Lungs isolated at *E*12.5 from two litters of *Tbx4-rtTA;tet-O-Cre;Srf*$^{fl/fl}$ mutants (7 lungs) and *Srf*$^{fl/fl}$ littermate controls (6 lungs) were dissected in sterile-filtered PBS, mechanically dissociated using fine tungsten needles (Fine Science Tools), and then further dissociated in dispase (Corning 354235) on ice for 15 minutes to create single-cell suspensions. Dispase was inactivated using DMEM/F12 medium (without HEPES) with 5% FBS and antibiotics (50 units/ml of penicillin and streptomycin) and the cell suspensions were passed through 40-μm-diameter mesh filters. scRNA-seq library preparation and sequencing were carried out by the Princeton Genomics Core Facility using the Chromium Single Cell 3’ Library and Gel Bead Kit v3 on the Chromium Controller (10X Genomics) following manufacturer protocols. Illumina sequencing libraries were prepared from the PCR-amplified cDNA from mutant lungs and controls using the Nextra DNA library prep kit (Illumina). Libraries were sequenced on a NovaSeq 6000 S Prime flowcell (Illumina) as paired-end 28 + 94 nucleotide reads, following manufacturer protocols. Base calling was performed and raw sequencing reads were filtered using the Illumina sequencer control software. The 10x CellRanger software version 3.0.2 was used to

run the count pipeline with default settings on all FASTQ files from each sample to generate gene-barcode matrices using the *Mus musculus* reference genome mm10-1.2.0. Data are available from GEO (GSE203171).

Alcian blue staining—Lungs isolated at *E*18.5 were dissected, fixed in 4% PFA in PBS for one hour, and then taken through a sucrose gradient prior to embedding and freezing in OCT (Tissue Tek) using dry ice. 10-μm-thick sections were obtained using a Leica CM3050S cryostat. Alcian blue staining and nuclear fast red counterstaining (Vector Laboratories H-3501) were carried out according to the manufacturer's protocol.

AFM—All AFM data were acquired with a JPK Nanowizard 3 Atomic Force Microscope driven by JPK Data Processing Software. We used Novascan probes consisting of a triangle-shaped silicon nitride cantilever and a silicon dioxide sphere with a radius of 2.5 μm. As reported by the manufacturer, the nominal specifications of the cantilever are a spring constant of 0.06 N/m, a length of 205 μm, a width of 25 μm, and a thickness of 0.6 μm. Lungs were dissected, embedded in OCT, frozen on dry ice, and cut into 10-μm-thick slices on a Leica CM3050S cryostat. Slices were immediately immersed in a chamber of PBS and put under the AFM. The spring constant of each probe was measured in PBS with the JPK software using the thermal noise method[38].

QUANTIFICATION AND STATISTICAL ANALYSES

scRNA-seq analysis—scRNA-seq data were imported into R and processed using the Seurat package following the recommended pipeline[39]. Clusters and expression levels of genes of interest were visualized using the uniform manifold approximation and projection (UMAP) dimensional reduction. Datasets from control and mutant lungs were processed first separately and then together, using the Seurat integration tools. KEGG enrichment analysis was performed on markers for smooth muscle clusters from mutants and controls using the clusterProfiler package in R[40]. To compare clusters between datasets, we carried out Pearson correlation analysis on gene expression profiles for pairs of clusters, then performed unsupervised hierarchical clustering. Diffusion analyses were carried out using the Destiny package in R[31]. First, we computationally isolated mesenchymal cells from the control dataset and merged them with the smooth muscle cells of the mutant dataset. The resultant Seurat object was passed through the FindVariableFeatures and ScaleData functions. Diffusion analysis was performed on only the control cells, followed by projection of the mutant cells onto the existing diffusion map. Diffusion analysis was also separately carried out on the mesenchymal and smooth muscle cells of the mutant dataset.

Image and statistical analyses—Quantifications of airway diameter, projected epithelial and whole lung areas, and number of terminal branches were made manually in Image J[41] and compared using a two-sided t-test in GraphPad Prism. For immunofluorescence analysis, intensity profiles were measured either around the airways and plotted in polar coordinates or along lines emanating from the epithelium using simple MATLAB pipelines. Images were first background subtracted and then average pixel intensities in 16 by 16 pixel (5.76 by 5.76 μm) windows were measured along contours or lines. For intensities measured around the airway epithelium, we compared

the mean intensity along the contour of mutants and controls using a two-sided t-test in MATLAB. Fibronectin intensity was measured manually at branch tips in Fiji and normalized to background. For intensities measured along a line emanating from the epithelium, we compared mutants and controls by two-way ANOVA in GraphPad Prism. For Ki67 immunofluorescence and EdU analysis, we measured the nuclear intensity of Ki67 or EdU in the mesenchyme adjacent to the primary bronchus between L.L1 and L.L2 or, for EdU experiments, in αSMA$^+$ cells (in controls) and αSMA$^-$ Sox9$^+$ cells (in mutants) around the primary bronchus between L.L1 and L.L2. Background intensity was subtracted, and 20 nuclei were measured per lung.

AFM analysis—Force curves were acquired with 0.5-nm resolution over a maximum distance of 2500 nm or force of 5 nN. Data points from the first 250 nm of each curve were fit in Matlab using the Hertz model,

$$F = \frac{4}{3}\frac{E}{1-\mu^2}R^{3/2}\delta^{3/2} + C$$

where F is the measured force, R the radius of the probe, δ the sample indentation, $\mu = 0.5$ the Poisson ratio, E the elastic modulus, and C a constant to appropriately shift the fit to the data. The limited fit range was applied because the Hertz model is valid for sample indentations significantly smaller than the sample thickness (10 μm) or the probe radius (2.5 μm).

Supplementary Material

Refer to Web version on PubMed Central for supplementary material.

Acknowledgements:

We thank Dr. Wei Wang and the Genomics Core Facility of Princeton University for assistance with transcriptomics. We are grateful to Dr. Wei Shi (Keck School of Medicine of USC) for generously providing us with the *Tbx4-rtTA;tet-O-Cre* mouse line. We thank the Confocal Imaging Facility, a Nikon Center of Excellence, in the Department of Molecular Biology at Princeton University for instrument use and technical advice. We are also grateful to members of the Tissue Morphodynamics Group for helpful discussions and feedback on the manuscript. This work was supported by the NIH (HD099030, HL120142, HL164861, and HD111539) and an HHMI Faculty Scholars Award to C.M.N. K.G. was supported in part by a postgraduate scholarship-doctoral (PGS-D) from the Natural Sciences and Engineering Research Council of Canada, the Dr. Margaret McWilliams Predoctoral Fellowship from the Canadian Federation of University Women, the Princeton University Procter Fellowship, and an American Heart Association Predoctoral Fellowship. P.Z. was supported by a PBI2 Scholar Award.

Abbreviations:

αSMA	α-smooth muscle actin
Bmp4	bone morphogenetic protein 4
Ecad	E-cadherin
Lef1	lymphoid enhancer binding factor 1

pMLC	phosphorylated myosin light chain
SRF	serum response factor
Tbx3	T-box transcription factor 3

References

1. Jaslove JM, and Nelson CM (2018). Smooth muscle: a stiff sculptor of epithelial shapes. Philos Trans R Soc Lond B Biol Sci 373. 10.1098/rstb.2017.0318.
2. Donadon M, and Santoro MM (2021). The origin and mechanisms of smooth muscle cell development in vertebrates. Development 148. 10.1242/dev.197384.
3. Owens GK, Kumar MS, and Wamhoff BR (2004). Molecular regulation of vascular smooth muscle cell differentiation in development and disease. Physiol Rev 84, 767–801. 10.1152/physrev.00041.2003. [PubMed: 15269336]
4. Rensen SS, Doevendans PA, and van Eys GJ (2007). Regulation and characteristics of vascular smooth muscle cell phenotypic diversity. Neth Heart J 15, 100–108. 10.1007/BF03085963. [PubMed: 17612668]
5. Wang G, Jacquet L, Karamariti E, and Xu Q (2015). Origin and differentiation of vascular smooth muscle cells. J Physiol 593, 3013–3030. 10.1113/JP270033. [PubMed: 25952975]
6. Yap C, Mieremet A, de Vries CJM, Micha D, and de Waard V (2021). Six Shades of Vascular Smooth Muscle Cells Illuminated by KLF4 (Kruppel-Like Factor 4). Arterioscler Thromb Vasc Biol 41, 2693–2707. 10.1161/ATVBAHA.121.316600. [PubMed: 34470477]
7. Du KL, Ip HS, Li J, Chen M, Dandre F, Yu W, Lu MM, Owens GK, and Parmacek MS (2003). Myocardin is a critical serum response factor cofactor in the transcriptional program regulating smooth muscle cell differentiation. Mol Cell Biol 23, 2425–2437. 10.1128/MCB.23.7.2425-2437.2003. [PubMed: 12640126]
8. Wang Z, Wang DZ, Pipes GC, and Olson EN (2003). Myocardin is a master regulator of smooth muscle gene expression. Proc Natl Acad Sci U S A 100, 7129–7134. 10.1073/pnas.1232341100. [PubMed: 12756293]
9. Chen J, Kitchen CM, Streb JW, and Miano JM (2002). Myocardin: a component of a molecular switch for smooth muscle differentiation. J Mol Cell Cardiol 34, 1345–1356. 10.1006/jmcc.2002.2086. [PubMed: 12392995]
10. Miano JM (2015). Myocardin in biology and disease. J Biomed Res 29, 3–19. 10.7555/JBR.29.20140151. [PubMed: 25745471]
11. Arsenian S, Weinhold B, Oelgeschlager M, Ruther U, and Nordheim A (1998). Serum response factor is essential for mesoderm formation during mouse embryogenesis. EMBO J 17, 6289–6299. 10.1093/emboj/17.21.6289. [PubMed: 9799237]
12. Li S, Wang DZ, Wang Z, Richardson JA, and Olson EN (2003). The serum response factor coactivator myocardin is required for vascular smooth muscle development. Proc Natl Acad Sci U S A 100, 9366–9370. 10.1073/pnas.1233635100. [PubMed: 12867591]
13. Hoofnagle MH, Neppl RL, Berzin EL, Teg Pipes GC, Olson EN, Wamhoff BW, Somlyo AV, and Owens GK (2011). Myocardin is differentially required for the development of smooth muscle cells and cardiomyocytes. Am J Physiol Heart Circ Physiol 300, H1707–1721. 10.1152/ajpheart.01192.2010. [PubMed: 21357509]
14. Zhang JC, Kim S, Helmke BP, Yu WW, Du KL, Lu MM, Strobeck M, Yu Q, and Parmacek MS (2001). Analysis of SM22alpha-deficient mice reveals unanticipated insights into smooth muscle cell differentiation and function. Mol Cell Biol 21, 1336–1344. 10.1128/MCB.2001.21.4.1336-1344.2001. [PubMed: 11158319]
15. Feng HZ, Wang H, Takahashi K, and Jin JP (2019). Double deletion of calponin 1 and calponin 2 in mice decreases systemic blood pressure with blunted length-tension response of aortic smooth muscle. J Mol Cell Cardiol 129, 49–57. 10.1016/j.yjmcc.2019.01.026. [PubMed: 30707993]

16. Schildmeyer LA, Braun R, Taffet G, Debiasi M, Burns AE, Bradley A, and Schwartz RJ (2000). Impaired vascular contractility and blood pressure homeostasis in the smooth muscle alpha-actin null mouse. FASEB J 14, 2213–2220. 10.1096/fj.99-0927com. [PubMed: 11053242]

17. Goodwin K, Jaslove JM, Tao H, Zhu M, Hopyan S, and Nelson CM (2022). Patterning the embryonic pulmonary mesenchyme. iScience 25, 103838. 10.1016/j.isci.2022.103838. [PubMed: 35252804]

18. He H, Huang M, Sun S, Wu Y, and Lin X (2017). Epithelial heparan sulfate regulates Sonic Hedgehog signaling in lung development. PLoS Genet 13, e1006992. 10.1371/journal.pgen.1006992. [PubMed: 28859094]

19. Boucherat O, Landry-Truchon K, Berube-Simard FA, Houde N, Beuret L, Lezmi G, Foulkes WD, Delacourt C, Charron J, and Jeannotte L (2015). Epithelial inactivation of Yy1 abrogates lung branching morphogenesis. Development 142, 2981–2995. 10.1242/dev.120469. [PubMed: 26329601]

20. Yi L, Domyan ET, Lewandoski M, and Sun X (2009). Fibroblast growth factor 9 signaling inhibits airway smooth muscle differentiation in mouse lung. Dev Dyn 238, 123–137. 10.1002/dvdy.21831. [PubMed: 19097117]

21. Goodwin K, Mao S, Guyomar T, Miller E, Radisky DC, Kosmrlj A, and Nelson CM (2019). Smooth muscle differentiation shapes domain branches during mouse lung development. Development 146. 10.1242/dev.181172.

22. Jaslove JM, Goodwin K, Sundarakrishnan A, Spurlin JW, Mao S, Kosmrlj A, and Nelson CM (2022). Transmural pressure signals through retinoic acid to regulate lung branching. Development 149. 10.1242/dev.199726.

23. Kim HY, Pang MF, Varner VD, Kojima L, Miller E, Radisky DC, and Nelson CM (2015). Localized Smooth Muscle Differentiation Is Essential for Epithelial Bifurcation during Branching Morphogenesis of the Mammalian Lung. Dev Cell 34, 719–726. 10.1016/j.devcel.2015.08.012. [PubMed: 26387457]

24. Young RE, Jones MK, Hines EA, Li R, Luo Y, Shi W, Verheyden JM, and Sun X (2020). Smooth Muscle Differentiation Is Essential for Airway Size, Tracheal Cartilage Segmentation, but Dispensable for Epithelial Branching. Dev Cell 53, 73–85 e75. 10.1016/j.devcel.2020.02.001. [PubMed: 32142630]

25. Zhang W, Menke DB, Jiang M, Chen H, Warburton D, Turcatel G, Lu CH, Xu W, Luo Y, and Shi W (2013). Spatial-temporal targeting of lung-specific mesenchyme by a Tbx4 enhancer. BMC Biol 11, 111. 10.1186/1741-7007-11-111. [PubMed: 24225400]

26. De Langhe SP, Sala FG, Del Moral PM, Fairbanks TJ, Yamada KM, Warburton D, Burns RC, and Bellusci S (2005). Dickkopf-1 (DKK1) reveals that fibronectin is a major target of Wnt signaling in branching morphogenesis of the mouse embryonic lung. Dev Biol 277, 316–331. 10.1016/j.ydbio.2004.09.023. [PubMed: 15617677]

27. Sakai T, Larsen M, and Yamada KM (2003). Fibronectin requirement in branching morphogenesis. Nature 423, 876–881. 10.1038/nature01712. [PubMed: 12815434]

28. Sieck GC, Dogan M, Young-Soo H, Osorio Valencia S, and Delmotte P (2019). Mechanisms underlying TNFalpha-induced enhancement of force generation in airway smooth muscle. Physiol Rep 7, e14220. 10.14814/phy2.14220. [PubMed: 31512410]

29. Luo L, Wang L, Pare PD, Seow CY, and Chitano P (2019). The Huxley crossbridge model as the basic mechanism for airway smooth muscle contraction. Am J Physiol Lung Cell Mol Physiol 317, L235–L246. 10.1152/ajplung.00051.2019. [PubMed: 31116578]

30. Gunst SJ, and Zhang W (2008). Actin cytoskeletal dynamics in smooth muscle: a new paradigm for the regulation of smooth muscle contraction. Am J Physiol Cell Physiol 295, C576–587. 10.1152/ajpcell.00253.2008. [PubMed: 18596210]

31. Haghverdi L, Buettner F, and Theis FJ (2015). Diffusion maps for high-dimensional single-cell analysis of differentiation data. Bioinformatics 31, 2989–2998. 10.1093/bioinformatics/btv325. [PubMed: 26002886]

32. Augstein A, Mierke J, Poitz DM, and Strasser RH (2018). Sox9 is increased in arterial plaque and stenosis, associated with synthetic phenotype of vascular smooth muscle cells and causes

alterations in extracellular matrix and calcification. Biochim Biophys Acta Mol Basis Dis 1864, 2526–2537. 10.1016/j.bbadis.2018.05.009. [PubMed: 29777903]

33. Wang L, Rice M, Swist S, Kubin T, Wu F, Wang S, Kraut S, Weissmann N, Bottger T, Wheeler M, et al. (2021). BMP9 and BMP10 Act Directly on Vascular Smooth Muscle Cells for Generation and Maintenance of the Contractile State. Circulation 143, 1394–1410. 10.1161/CIRCULATIONAHA.120.047375. [PubMed: 33334130]
34. Chettimada S, Joshi SR, Dhagia V, Aiezza A 2nd, Lincoln TM, Gupte R, Miano JM, and Gupte SA (2016). Vascular smooth muscle cell contractile protein expression is increased through protein kinase G-dependent and -independent pathways by glucose-6-phosphate dehydrogenase inhibition and deficiency. Am J Physiol Heart Circ Physiol 311, H904–H912. 10.1152/ajpheart.00335.2016. [PubMed: 27521420]
35. Andrikopoulos K, Suzuki HR, Solursh M, and Ramirez F (1992). Localization of pro-alpha 2(V) collagen transcripts in the tissues of the developing mouse embryo. Dev Dyn 195, 113–120. 10.1002/aja.1001950205. [PubMed: 1297453]
36. Ng LJ, Wheatley S, Muscat GE, Conway-Campbell J, Bowles J, Wright E, Bell DM, Tam PP, Cheah KS, and Koopman P (1997). SOX9 binds DNA, activates transcription, and coexpresses with type II collagen during chondrogenesis in the mouse. Dev Biol 183, 108–121. 10.1006/dbio.1996.8487. [PubMed: 9119111]
37. Carraro G, del Moral PM, and Warburton D (2010). Mouse embryonic lung culture, a system to evaluate the molecular mechanisms of branching. J Vis Exp. 10.3791/2035.
38. Hutter JL, and Bechhoefer J (1993). Calibration of atomic-force microscope tips. Review of Scientific Instruments 64, 1868–1873. 10.1063/1.1143970.
39. Butler A, Hoffman P, Smibert P, Papalexi E, and Satija R (2018). Integrating single-cell transcriptomic data across different conditions, technologies, and species. Nat Biotechnol 36, 411–420. 10.1038/nbt.4096. [PubMed: 29608179]
40. Yu G, Wang LG, Han Y, and He QY (2012). clusterProfiler: an R package for comparing biological themes among gene clusters. OMICS 16, 284–287. 10.1089/omi.2011.0118. [PubMed: 22455463]
41. Schneider CA, Rasband WS, and Eliceiri KW (2012). NIH Image to ImageJ: 25 years of image analysis. Nat Methods 9, 671–675. 10.1038/nmeth.2089. [PubMed: 22930834]

Highlights

- Contractile smooth muscle marker genes require mesenchymal *Srf* in the embryonic lung.
- *Srf*-mutant mesenchyme exhibits normal patterning and mechanical properties.
- Mutant “smooth muscle” wraps the airways and expresses wildtype smooth muscle genes.
- *Srf* deletion leads to the formation of synthetic smooth muscle rather than contractile.

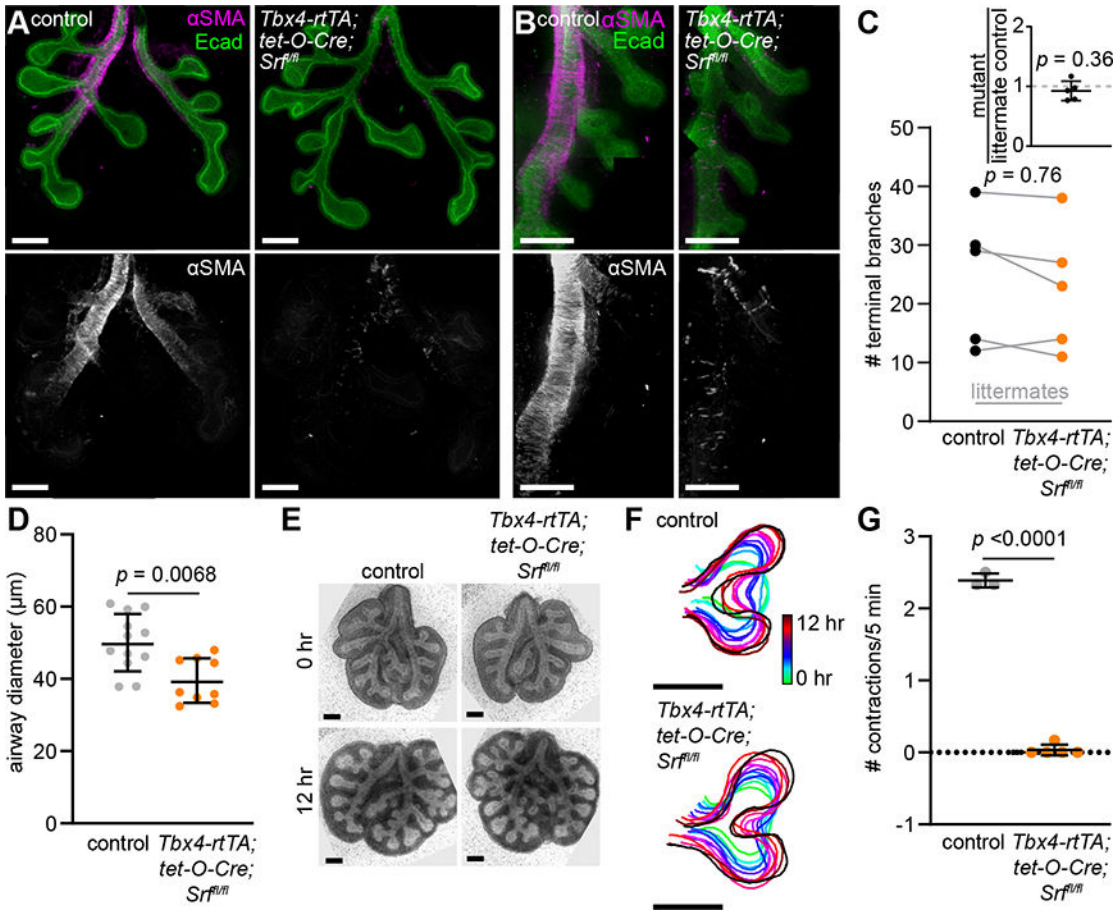

Figure 1. Deleting *Srf* from the embryonic pulmonary mesenchyme leads to loss of αSMA but does not affect epithelial branching.

(**A-B**) *E*12.5 *Tbx4-rtTA;tet-O-Cre;Srf*$^{fl/fl}$ and littermate control lungs immunostained for Ecad and αSMA. Scale bars, 100 μm. (**C**) Number of branches in *E*12.5 *Tbx4-rtTA;tet-O-Cre;Srf*$^{fl/fl}$ and littermate control lungs, connected by gray lines and compared using a t-test. Inset shows branch number in mutant lungs divided by that of littermate controls compared to a hypothetical mean of 1 using a one sample t-test. Error bars show s.d. (**D**) Airway diameter measured between the first two domain branches of the left lobe of *E*12.5 *Tbx4-rtTA;tet-O-Cre;Srf*$^{fl/fl}$ lungs and controls (n = 12 controls, 9 mutants). (**E**) Brightfield images of *E*12.5 *Tbx4-rtTA;tet-O-Cre;Srf*$^{fl/fl}$ and littermate control lungs cultured *ex vivo*. Scale bars, 200 μm. (**F**) Contours of the epithelium showing dynamic changes in the morphology of terminal bifurcations in mutants and controls. Scale bars, 50 μm. (**G**) Number of spontaneous smooth muscle contractions per five-minute timelapse in *Tbx4-rtTA;tet-O-Cre;Srf*$^{fl/fl}$ and littermate control lungs (n = 3 controls, 5 mutants). Error bars show s.d. Groups were compared using two-sided t-test.

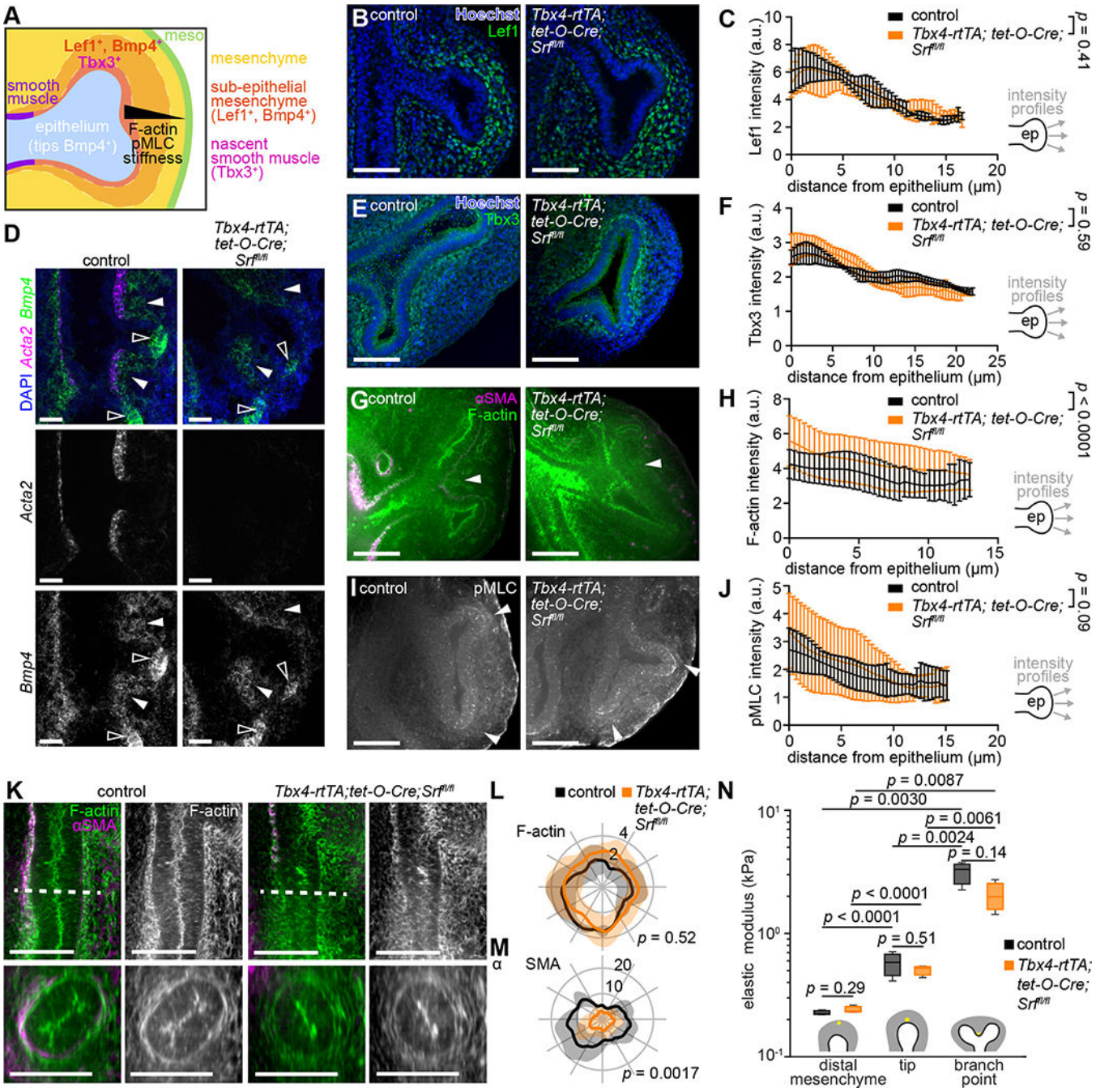

Figure 2. *Srf*-mutant lungs exhibit normal mesenchymal patterning.

(**A**) Schematic illustrating the expected patterns of cytoskeletal elements, tissue mechanical properties, and markers of patterning in the mesenchyme around epithelial tips. (**B-C**) *E*12.5 control and *Tbx4-rtTA;tet-O-Cre;Srf*$^{fl/fl}$ lungs immunostained for Lef1 and counterstained with Hoechst and quantification of Lef1 intensity profiles around epithelial buds (n = 3 controls, 3 mutants). Mean and s.d. are plotted and curves were compared using two-way ANOVA. Schematic shows lines and direction along which intensity profiles were measured. (**D**) RNAscope analysis of *Acta2* and *Bmp4* on sections of *E*12.5 control

and *Tbx4-rtTA;tet-O-Cre;Srf*$^{fl/fl}$ lungs. Filled arrowheads indicate *Bmp4*$^{+}$ sub-epithelial mesenchyme and empty arrowheads indicate *Bmp4*$^{+}$ epithelial tips. (**E-F**) *E*12.5 control and *Tbx4-rtTA;tet-O-Cre;Srf*$^{fl/fl}$ lungs immunostained for Tbx3 and counterstained with Hoechst and quantification of Tbx3 intensity profiles around epithelial tips (n = 3 controls, 3 mutants). Mean and s.d. are plotted and curves were compared using two-way ANOVA. (**G-J**) *E*12.5 control and *Tbx4-rtTA;tet-O-Cre;Srf*$^{fl/fl}$ lungs immunostained for αSMA and F-actin or pMLC and quantification of F-actin and pMLC intensity profiles around epithelial tips (n = 9 controls, 11 mutants for F-actin; n = 4 controls, 6 mutants for pMLC). Arrowhead indicates enrichment of mesenchymal F-actin and pMLC near the branching epithelium. (**K**) Single confocal slices and reconstructed optical cross-sections through *E*12.5 control and *Tbx4-rtTA;tet-O-Cre;Srf*$^{fl/fl}$ lungs immunostained for αSMA and F-actin. Dashed line indicates location of the cross-section. (**L-M**) Polar plots showing F-actin and αSMA intensity around the airways based on angle from the center of the bronchus in *E*12.5 control and *Tbx4-rtTA;tet-O-Cre;Srf*$^{fl/fl}$ lungs (n = 3 controls, 9 mutants). Line shows mean and shaded area shows s.d. *p* value is for comparison of mean intensities using two-sided t-test. (**N**) Elastic moduli of the regions of interest indicated by yellow circles in *E*12.5 *Tbx4-rtTA;tet-O-Cre;Srf*$^{fl/fl}$*;mTmG* lungs and controls (n = 3).

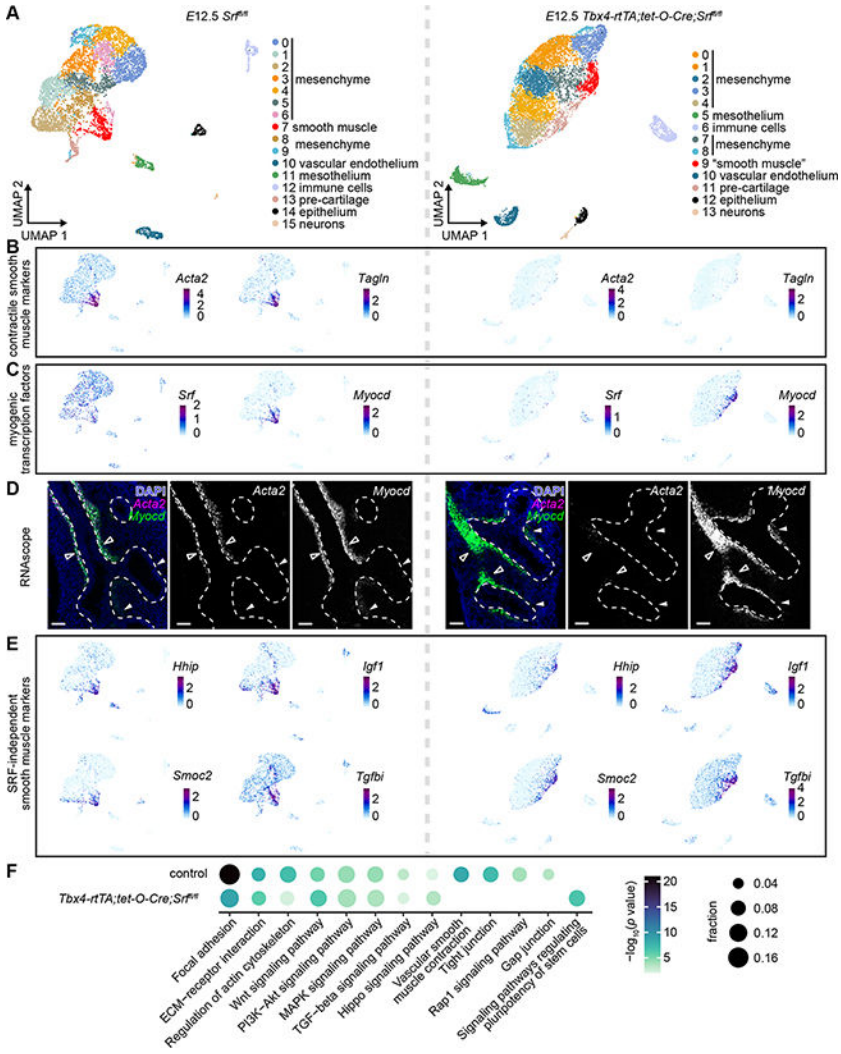

Figure 3. scRNA-seq identifies a smooth muscle-like population in *Srf*-mutant lungs.

(**A**) UMAPs of cells isolated from *E*12.5 *Tbx4-rtTA;tet-O-Cre;Srf*$^{fl/fl}$ and littermate control lungs color-coded according to cluster (n = 6 controls, 7 mutants). (**B-C**) Expression levels of *Acta2*, *Tagln*, *Srf* and *Myocd* in mutants and controls. (**D**) RNAscope analysis of *Acta2* and *Myocd* in *E*12.5 *Tbx4-rtTA;tet-O-Cre;Srf*$^{fl/fl}$ and littermate control lungs. Dashed lines outline the epithelium. Filled arrowheads point to branch tips and empty arrowheads point to branch stalks. Scale bars, 50 μm. (**E**) Expression levels of *Hhip*, *Igf1*, *Smoc2*, and *Tgfbi* in mutants and controls. (**F**) KEGG pathway enrichment analysis for marker genes of the smooth muscle clusters from control and *Tbx4-rtTA;tet-O-Cre;Srf*$^{fl/fl}$ lungs.

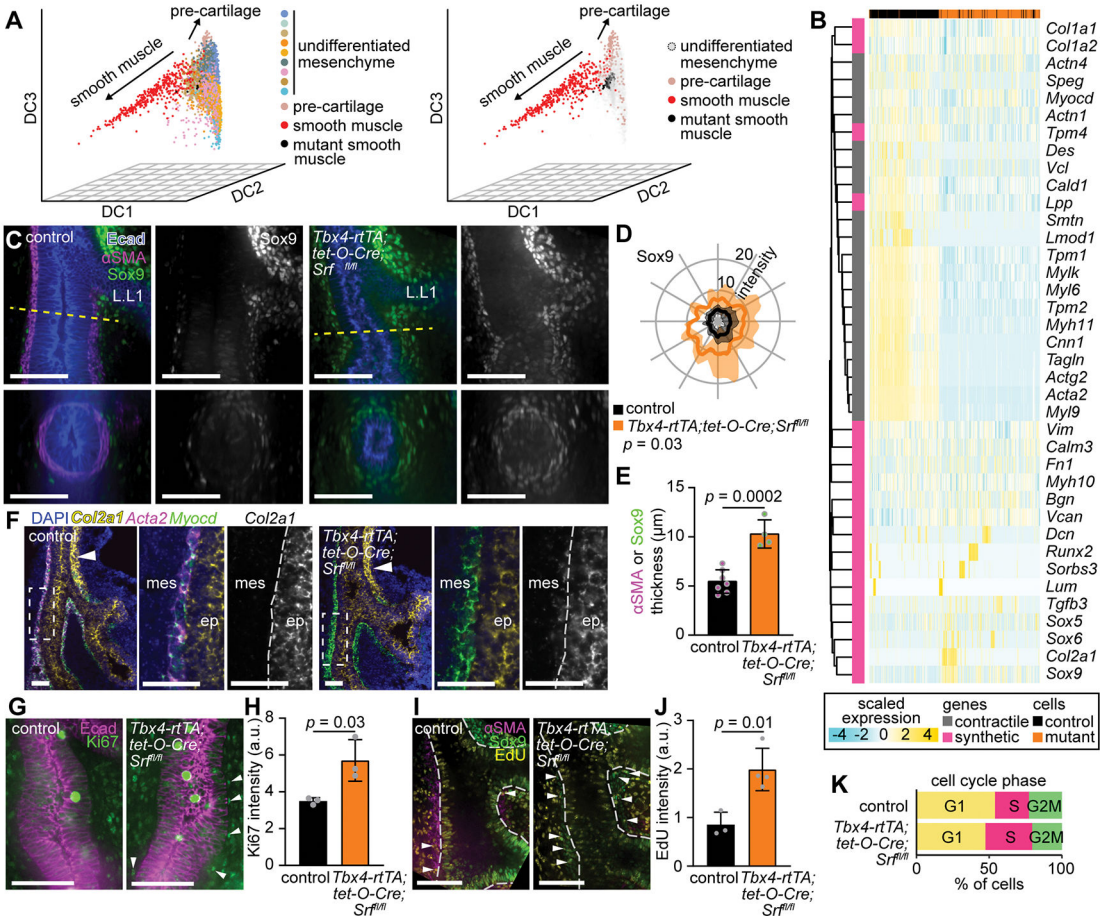

Figure 4. *Srf*-null airway smooth muscle cells display a phenotype consistent with synthetic smooth muscle.

(**A**) Diffusion analysis of mesenchymal cells from the control dataset and projection of *Tbx4-rtTA;tet-O-Cre;Srf*$^{fl/fl}$ mutant smooth muscle cells onto the diffusion map. Left plot is color-coded according to clusters from Fig. 3A; right plot is color-coded to emphasize control and mutant smooth muscle and cartilage precursors. (**B**) Clustering of mutant and control smooth muscle cells based on expression of genes associated with contractile or synthetic smooth muscle phenotype. (**C**) Single confocal slices and reconstructed optical cross-sections through *E*12.5 control and *Tbx4-rtTA;tet-O-Cre;Srf*$^{fl/fl}$ lungs immunostained for Ecad, αSMA, and Sox9. Dashed line indicates location of the reconstructed cross-section. (**D**) Polar plots showing Sox9 intensity around the airways based on angle from the center of the bronchus of *E*12.5 control and *Tbx4-rtTA;tet-O-Cre;Srf*$^{fl/fl}$ lungs (n = 5 controls, 2 mutants). Line shows mean and shaded area shows s.d. *p* value is for the comparison of mean intensities using two-sided t-test. (**E**) Thickness of αSMA^{+} cell layer in controls and Sox9^{+} cell layer in mutants compared by t-test (n = 7 controls, 4 mutants). (**F**) RNAscope analysis of *Acta2*, *Myocd*, and *Col2a1* on sections of *E*12.5 control and *Tbx4-rtTA;tet-O-Cre;Srf*$^{fl/fl}$ lungs. Arrowheads indicate *Col2a1*$^{+}$ cartilage precursors along lateral side of the primary bronchus. Dashed boxes indicate zoomed-in regions shown to the right. Gray dashed line indicates border between the mesenchyme (mes) and epithelium (ep). (**G**) Single confocal slices of *E*12.5 control and *Tbx4-rtTA;tet-O-Cre;Srf*$^{fl/fl}$ lungs

immunostained for Ecad and Ki67. Arrowheads point to smooth muscle cells with high Ki67 intensity. (**H**) Quantification of nuclear Ki67 intensity in smooth muscle cells of mutants and controls compared by t-test (n = 3). (**I**) Single confocal slices of *E*12.5 control and *Tbx4-rtTA;tet-O-Cre;Srf*$^{fl/fl}$ lungs immunostained for αSMA and Sox9 after a 15 min EdU pulse, focused on the primary bronchus between L.L1 and L.L2. White dashed line indicates border of the epithelium. Arrowheads point to smooth muscle cells with high EdU intensity. (**J**) Quantification of EdU intensity in smooth muscle cells of mutants and controls compared by t-test (n = 3–4). (**K**) Percentages of control and *Tbx4-rtTA;tet-O-Cre;Srf*$^{fl/fl}$ smooth muscle cells at each phase of the cell cycle based on scRNA-seq data. Scale bars, 50 μm.

Key resources table

REAGENT or RESOURCE	SOURCE	IDENTIFIER
Antibodies		
Mouse monoclonal αSMA antibody	Sigma	a5228
Rabbit polyclonal αSMA antibody	Abcam	ab5694
Rabbit monoclonal E-cadherin antibody	Cell Signaling	3195
Rat monoclonal E-cadherin antibody	Invitrogen	13-1900
Rabbit monoclonal fibronectin antibody	Invitrogen	PA5-29578
Rabbit monoclonal Lef1 antibody	Cell Signaling	2230
Rabbit polyclonal to Ki67	Abacom	ab15580
Rabbit polyclonal pMLC antibody	Cell Signaling	3671
Rabbit polyclonal RFP antibody	Abcam	ab62341
Rabbit polyclonal Sox9 antibody	Sigma	AB5535
Rabbit polyclonal Tbx3 antibody	Invitrogen	42-4800
Goat anti-Mouse IgG1 Cross-Adsorbed Secondary Antibody, Alexa Fluor 647	Invitrogen	A-21240
Goat anti-Rat IgG (H+L) Cross-Adsorbed Secondary Antibody, Alexa Fluor 488	Invitrogen	A-11006
Goat anti-Rat IgG (H+L) Cross-Adsorbed Secondary Antibody, Alexa Fluor 594	Invitrogen	A-11007
Goat anti-Rabbit IgG (H+L) Cross-Adsorbed Secondary Antibody, Alexa Fluor 594	Invitrogen	A-11012
Goat anti-Rabbit IgG (H+L) Cross-Adsorbed Secondary Antibody, Alexa Fluor 647	Invitrogen	A-21244
Alexa Fluor 568 Phalloidin	Thermo Fisher Scientific	A12380
Alexa Fluor 488 Phalloidin	Thermo Fisher Scientific	A12379
Critical commercial assays		
RNAScope Multiplex Fluorescent V2 Assay	ACD	Cat No. 323100
RNAScope Probe Mm-Myocd	ACD	581051
RNAScope Probe Mm-Col2a1	ACD	407221
RNAScope Probe Mm-Bmp4	ACD	401301
RNAScope Probe Mm-Acta2	ACD	319531
Alcian blue stain kit	Vector Laboratories	H-3501
Deposited data		
Raw and analyzed scRNA-seq data of *E*12.5 *Tbx4-rtTA;tet-O-Cre;SRF$^{fl/fl}$* mutant and *SRF$^{fl/fl}$* littermate controls lungs	This paper	GEO: GSE203171
Experimental models: Organisms/strains		
Mouse: *Srf^{tm1Rmn}*/J	The Jackson Laboratory	JAX: 006658
Mouse: *Tbx4-rtTA*	Gift from Wei Shi (USC)	N/A
Mouse: *tet-O-Cre*	The Jackson Laboratory	JAX: 006234
Oligonucleotides		

REAGENT or RESOURCE	SOURCE	IDENTIFIER
Primer: Cre, Forward: GCATTACCGGTCGATGCAACGAGTGATGAG	Devenport Lab (Princeton University)	N/A
Primer: Cre, Reverse: GAGTGAACGAACCTGGTCGAAATCAGTGCG	Devenport Lab (Princeton University)	N/A
Primer: Tbx4, Forward: CGGCCCCGAATTCACCATGTCTAGA	Zhang et al.[25]	N/A
Primer: Tbx4, Reverse: ACGCGTCGACACTTAGTTACCCGGGGAGCATG	Zhang et al.[25]	N/A
Primer: SRF-flox, Forward: TGCTTACTGGAAAGCTCATGG	The Jackson Laboratory	Primer no. oIMR6490
Primer: SRF-flox, Reverse: TGCTGGTTTGGCATCAACT	The Jackson Laboratory	Primer no. oIMR6491
Software and algorithms		
ImageJ	Schneider et al.[41]	https://imagej.nih.gov/ij/
MATLAB	MathWorks	N/A
CellRanger	10X Genomics	Version 3.0.2
R	R Foundation for Statistical Computing	N/A
Seurat	Butler et al.[39]	https://satijalab.org/seurat/
Destiny	Haghverdi et al.[31]	https://www.bioconductor.org/packages/release/bioc/html/destiny.html
Other		
Opal Polaris 480 Reagent Pack	Akoya Biosciences	FP1500001KT
Opal 520 Reagent Pack	Akoya Biosciences	FP1487001KT
Opal 650 Reagent Pack	Akoya Biosciences	FP1495001KT
RNaseZAP	Sigma	R2020